

Amorphous Steel Enabled Anode-Free, Thin-Film Li-Ion μ -Battery

Daba Deme Megersa, Gutema Teshome Gudena, Youngho Kim, Ji Kwon Bae, Jaeyeong Lee, and Hak Ki Yu*

This work presents a less than 1.3 μm thick, low-cost, and ambient-condition-processable Li-ion μ -battery by transforming stainless steel (SS) which is the structural battery component into a multifunctional current collector and the anode. Radio frequency (rf) sputtering of SS under room temperature (RT) and moderate vacuum forms amorphous mix of metal, carbon, and metal oxide providing both electrical conductivity and the ability to host lithium ions. This novel approach breaks the predominant use of SS as a structural component. The full-cell anode-free-all-solid-state μ -battery is fabricated using an RT, layer-by-layer rf-sputtering process, depositing SS, lithium iron phosphate (LiFePO_4), and

lithium phosphate (Li_3PO_4) on a silicon wafer. Probing into the μ -battery using time-of-flight secondary ion mass spectrometry confirms successful plating and stripping of lithium on the amorphous SS during cycling and the formation of solid electrolyte interface. A real-time test demonstrates that a single cell μ -battery powers a red-light emitting diode for μ -seconds. This work demonstrates the feasibility of designing a functional μ -battery on a silicon wafer using only two common battery materials and one structural material, eliminating the need for complex procedures. The battery can seamlessly integrate into circuits of micro-power sources for low-power devices.

1. Introduction

All solid-state thin-film Li-ion μ -batteries are a promising candidate to power tiny devices in microelectronics and the Internet of Things due to their compatible size, capacity, and safety.^[1–3] The early version of μ -batteries are thin film batteries (TFB) such as Ag/Li/Li, $\text{TiS}_2/\text{Li}-\text{I}-\text{P}-\text{O}/\text{Li}$, and $\text{LiCoO}_2/\text{LiPON}/\text{Li}$, which have been in research for several decades.^[3] Enormous

focus has been given to high ionic conductivity solid electrolyte (SE) synthesis and control of solid electrolyte interface (SEI), which are bottlenecks to successful battery development.^[4–9] For instance cathode-electrolyte stabilization, coherent interface, and interphase engineering are demonstrated as successful methods to obtain a stable and high-capacity thin film battery.^[10–12] Major advances in terms of material development and battery architecture include successful development oxide-based SE using vapor deposition techniques, 3D TFP, flexible TFB, and multi-layered TFB.^[7,9,13–19] Recently, artificial SEI layer was developed to control dendrite growth, and elastic electrolyte was developed for enhanced performance.^[20,21] More recently, quasi-solid-state and solid-state anode-free Li-ion batteries have demonstrated a high capacity and low cost.^[22,23]

Designing all-solid-state μ -batteries poses challenges due to the reliance on clean room setups and expensive materials, which increase cost and complexity, despite their good energy and power densities.^[24] To enhance practicality, the focus must shift toward creating μ -batteries that are affordable, ambient-processable, and adaptable, ensuring seamless integration into circuit systems while balancing performance and cost-effectiveness. Ultrathin anode-free μ -batteries have never been tried and could be one way to increase the capacity and cut cost.

To achieve this goal, we have developed a novel all-solid-state μ -battery using layer-by-layer rf-sputtering process at room temperature and in medium vacuum range. The μ -battery has a total thickness of less than 1.3 μm and mainly composed of only three materials which are best studied and widely commercialized. Thus, stainless steel (SS), LiFePO_4 , Li_3PO_4 , and SS were sequentially deposited onto a silicon wafer, forming the current collector, cathode, electrolyte, and anode/current collector, respectively. The multifunctional nature of SS, serving both as an anode and current collector, played a crucial role in making this design

D. Deme Megersa, G. T. Gudena, Y. Kim, H. K. Yu

Department of Energy Systems Research

Ajou University

Suwon 16499, South Korea

E-mail: hakkiyu@ajou.ac.kr

D. Deme Megersa, G. T. Gudena, Y. Kim, H. K. Yu

Department of Materials Science and Engineering

Ajou University

Suwon 16499, South Korea

J. K. Bae

Department of Materials Science and Engineering

Seoul National University

Seoul 08826, South Korea

Y. Kim

Department of Materials Science and Engineering

Korea University

Seoul 02841, South Korea

J. Lee

Korea Basic Science Institute

Busan Center

Busan 46742, South Korea



Supporting information for this article is available on the WWW under <https://doi.org/10.1002/batt.202500335>



© 2025 The Author(s). *Batteries & Supercaps* published by Wiley-VCH GmbH. This is an open access article under the terms of the Creative Commons Attribution License, which permits use, distribution and reproduction in any medium, provided the original work is properly cited.

feasible. Furthermore, multifunctionalization of SS breaks the long-standing practice of using SS only as structural component. By utilizing simple, low-cost materials, we have successfully created an anode-free all-solid-state μ -battery that operates under ambient conditions.

Probing into the μ -battery using time-of-flight secondary ion mass spectrometry (ToF-SIMS) provided insights into the distribution of Li-ions throughout the battery. The analysis confirmed that Li plating and stripping occurred during charging and discharging, validating the battery's operation. Additionally, the sputtering conditions for each component were optimized to achieve the desired properties. Importantly, we avoided clean room sample handling procedures throughout the entire process, making the study in near-practical scenarios. The μ -battery and its individual components were thoroughly characterized by HP-XRD, SEM, RAMAN spectroscopy, and electrochemical techniques, and the key findings are presented in this study. We believe this research lays the foundation for the alternative and cheap design of μ -batteries that can easily be integrated into microelectronics. Our ongoing efforts will focus on optimizing the battery's efficiency and energy density with the goal of making it a viable option for a wide range of applications.

2. Results and Discussion

The schematic diagram presented in Figure 1a demonstrates the steps used to prepare the anode-free-all-solid-state μ -battery. Silicon wafer was utilized as starting substrate; patterns were designed using lab-made aluminum mask followed by layer-by-layer rf-sputtering. Figure 1b,c depicts front and cross-sectional views of the battery composed of SS current collectors

LiFePO₄ cathode and Li₃PO₄ electrolyte. The architecture uses identical SS structures to sandwich active layer of the battery preventing air and moisture and extended SS arms for electrical contact. Figure 1d presents the digital camera image of the μ -battery.

Figure 1e shows an optical microscope image of the battery, the color difference is used to identify each layer of the battery including beneath silicon layer, green LiFePO₄, brown Li₃PO₄, and dark metallic SS surface. Figure 1f shows SEM cross-section image of the μ -battery in which the LiFePO₄ cathode and Li₃PO₄ solid-electrolyte (SE) are sandwiched between SS and confined to $\approx 1.2\ \mu\text{m}$. It can be observed that after successive layer-by-layer depositions, the obtained μ -battery maintains good structural integrity and individual components can be clearly observed. In addition, the LiFePO₄/Li₃PO₄ layer forms a brittle fracture while SS layer undergoes ductile fracture making easy identification of the layers. In Figure 2a, XRD pattern of the μ -battery in its pristine, charged, and discharged states is presented. It confirmed the amorphous nature of the battery with no significant change in structure during cycling.

Figure 2b presents several micrometer-wide SEM cross-section images of the μ -battery in full cell configuration and the marked interfaces between SS/SiO₂ (Figure 2c) and SS/LiFePO₄ (Figure 2d). It shows uniformly deposited SS with columnar structure, which was used as current collector as well as anode, and uniformly grown, smoothly interfaced LiFePO₄ which was used as a cathode active material. In Figure S1, Supporting Information, SEM-EDS elemental spectrum and corresponding elemental composition table of SS/SiO₂ are presented, confirming the presence of metal, carbon, and oxide species in the amorphous SS.

It is possible to speculate that amorphous layer of SS composed of metal, carbon, and metal oxide can serve as current collector and anode.^[25–27]

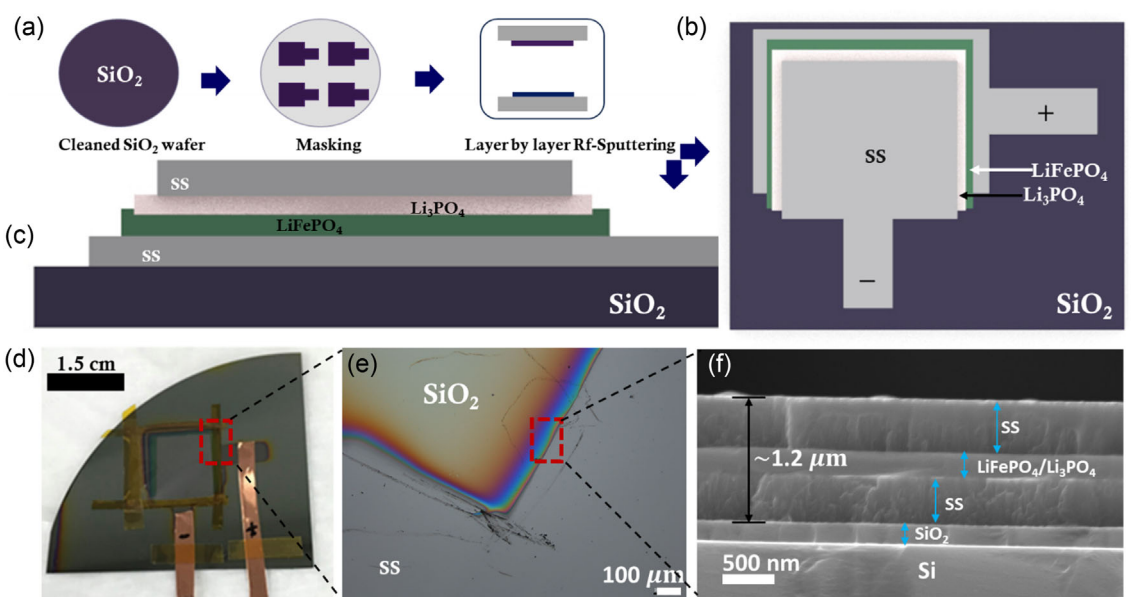


Figure 1. a) Simplified μ -battery fabrication route. b,c) Schematics of top and cross-sectional views of the μ -battery with details of material type and shape. d) Digital camera image of the prepared full cell μ -battery. e) Optical microscope image of the battery showing distinct color difference between several layers created by the μ -battery components. f) SEM cross-section image of the μ -battery clearly showing the dimension, fracture mechanism, and interface of each component.

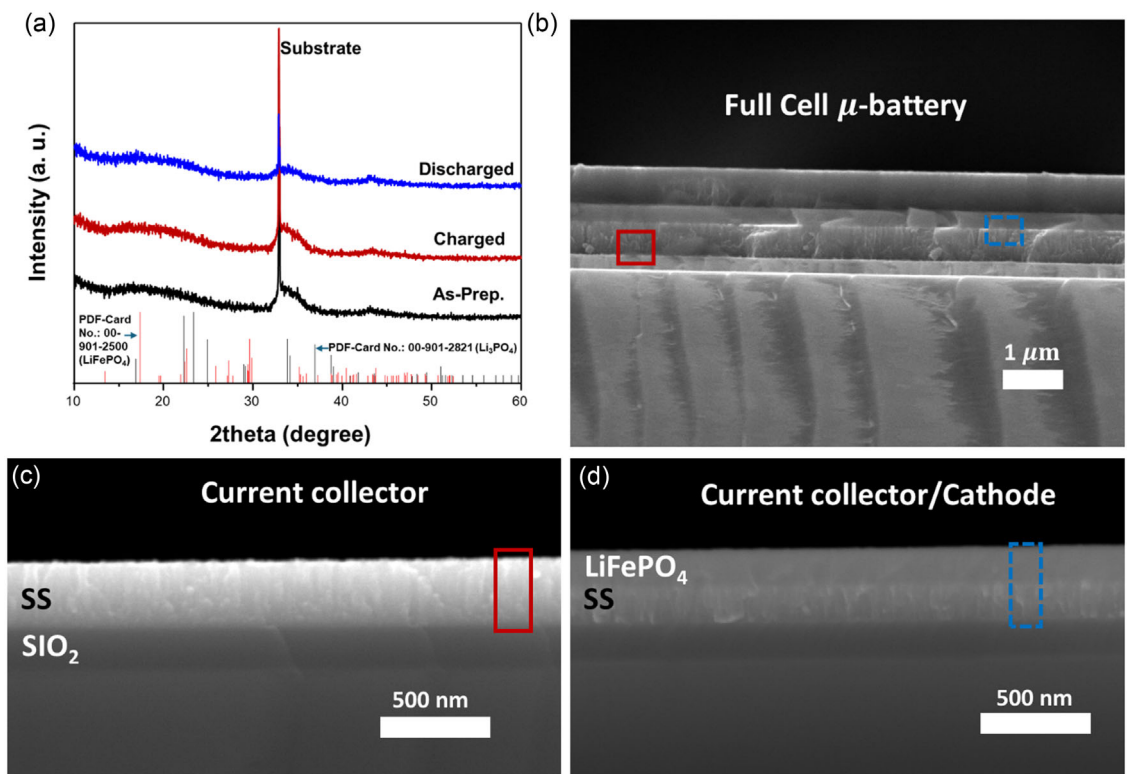


Figure 2. a) High power X-ray diffraction (HP-XRD) patterns of the μ -battery in pristine, charged, and discharged state, confirming the amorphous nature of the battery. SEM cross-section images of b) the μ -battery in full cell configuration showing SS sandwiched battery-active layer. c) Columnar stainless layer uniformly deposited on SiO_2 which served as current collector and anode. d) Uniformly deposited cathode active layer of LiFePO_4 on SS layer with tight contact and easily distinguishable via fracture mechanism difference.

After the structural integrity of the μ -battery was confirmed, to further explore the multifunctional nature of SS and the performance of the μ -battery, electrochemical analysis was conducted. Initially, the optimization of the SE charge transfer resistance was performed, and some interesting findings were observed. As the deposition temperature increased from RT to 300 °C, the Nyquist plot semi-circle increased one order of magnitude, indicating the drastic decrease in ionic conductivity (Figure S2, Supporting Information). Therefore, the full cell μ -battery was constructed utilizing Li_3PO_4 deposited at RT which provided the lowest charge transfer resistance of all. The result was in agreement with recent findings on the inverse correlation between crystallinity of LPO and its ionic conductivity.^[7] While in-depth EIS analysis of LPO according to depositional temperature will be the focus of our ongoing works, we have identified some interesting Nyquist plots which are in close agreement with the previous works. In addition, based on the architecture and microstructure of our battery, we have used the combinations of equivalent circuit elements to represent interfacial resistance, charge transfer resistance, constant phase element, and Warburg element.^[26–30] In addition, RT deposition the electrolyte might reduce interfacial reactions between cathode/electrolyte and electrolyte/SS layers.^[31,32]

In Figure 3a, digital camera image of the pristine μ -battery is presented; the extended arms of SS allowed easy contact with copper foil using silver paste as a binder; furthermore, the

packaging was done by polyethylene sheet and polyimide tape to prevent moisture and possible delamination of copper foil during testing. In Figure 3b, cyclic voltammetry (CV) scan of the pristine μ -battery acquired at scan rate of 5 mV s⁻¹ is presented. The scan clearly shows an oxidation peak around 3.2 V and partial reduction with no distinct peak. In Figure 3c, Nyquist plot of the pristine μ -battery is presented. The Nyquist curve has two consecutive semicircles at low and high frequency indicating contact resistance, double layer capacitance, and diffusion-controlled charge transfer behavior by $\text{LiFePO}_4/\text{Li}_3\text{PO}_4$. Figure 3d shows a digital camera image of a real-time test of the battery using a single cell was able to light a red 630 nm light-emitting diode LED (at the top center of the image) for a few milliseconds (see movie 1 and 2, Supporting Information). Figure S3, Supporting Information, presents the μ -battery prepared for initial activation which was charged 5 μA and discharged at $-2.5 \mu\text{A}$ for three cycles.

Furthermore, the μ -battery is tested for its capacity to store charge at several C-rates and presented in Figure 3e. The acquired charge/discharge curve starts by applying 0.6 μA , followed by several charging and discharging cycles at various currents. It was observed that for low C-rates of 0.75 C, the battery showed significantly stable discharge current for extended time, while for higher C-rates, the battery showed fast discharge. In Figure 3f, the stability test result is presented by charging the μ -battery at 10 μA and discharging at $-1 \mu\text{A}$ for 100 cycles;

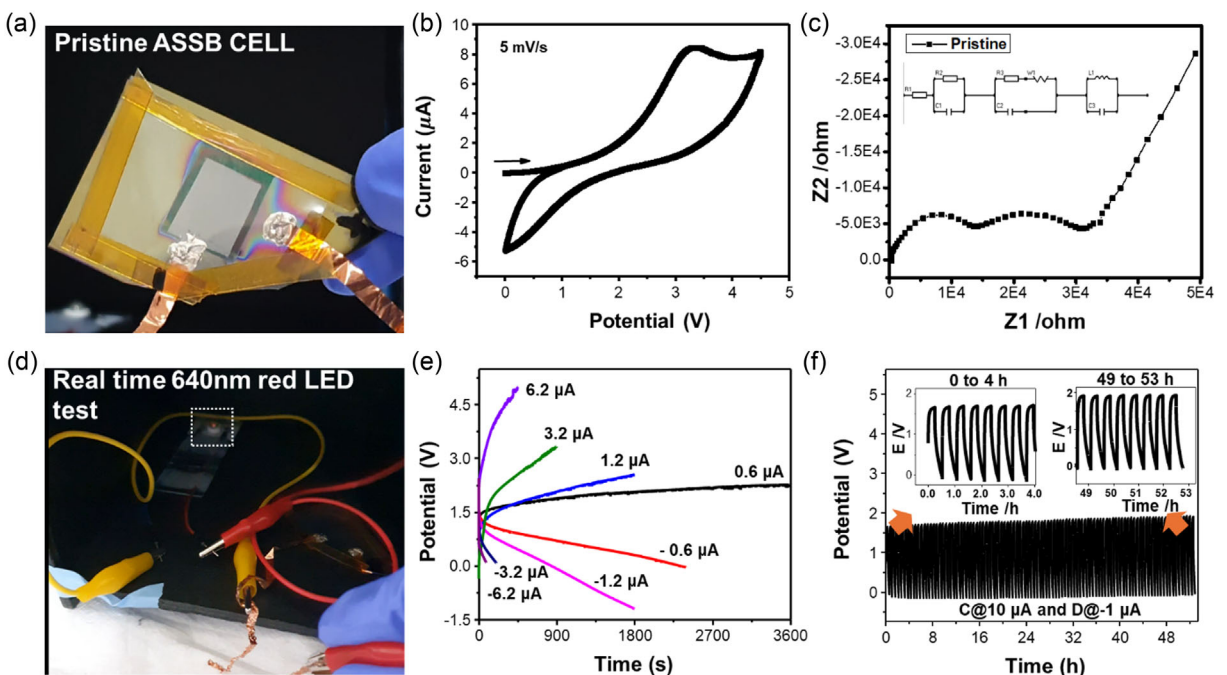


Figure 3. a) Digital camera image of single cell μ -battery with copper foil wiring and simple packaging. b) CV scan of the μ -battery in full cell configuration showing partially reversible redox peaks. c) EIS of pristine μ -battery in full cell configuration showing two distinct semicircles along with equivalent circuit diagram for charge transport behavior. d) Digital camera image of single cell μ -battery supplying enough power to light 640 nm red LED for several milliseconds. e) GCD test of μ -battery at various charging and discharging current. f) Stability test for 100 cycles.

there is no observable decay in capacity after cycling. Furthermore, the battery was cycled at C-rate of 1C, 2C, and 4C for 100 cycles each, and discharge capacity of first 6 cycles and last 6 cycles is presented in Figure S5a,b, Supporting Information. Quantitatively, as presented in Figure S5c, Supporting Information, for 1C, 2C, and 4C, initially average discharge capacity of 41.08, 41.27, and 40.35 mAh g⁻¹ was achieved, respectively, while at the final cycles, average discharge capacity of 39.47, 32.68, and 29.29 mAh g⁻¹ was achieved, respectively. Therefore, capacity retention of 1C was 96% followed by 79.18% of 2C and 72.5% of 4C. The result shows that the battery has outstanding capability at 1C and relatively good retention at other C-rates.

Real-time and electrochemical testing of the battery yielded interesting results, showing its ability to operate effectively for extended period, even after being stored in ambient conditions for over a year. This raises questions about the distribution of lithium in the pristine, fully charged, and discharged states, as well as how charge is stored in the SS anode, one of the least commonly used materials. To investigate this, ToF-SIMS analysis was conducted. Figure 4a–c presents video snapshot image of pristine, charged, and discharged μ -battery before and after ToF-SIMS analysis. The compact nature of the battery makes favorable sputtering for area of 300 μ m by 300 μ m characterized by smooth crater formation at the end of sputtering which lasted for 6030 s.

Figure 4d–f shows the 2D Li-ion distribution of the battery; there is a clear difference between the three states of the battery. Especially in charged state, there is observable accumulation of lithium ions evidenced by deep orange contrast and diminished contrast in discharged state showing the movement of Li-ion

away from the surface. Figure 4g–i shows 3D lithium-ion distribution profile in a pristine, charged, and discharged state. The 3D lithium-ion profile gives compelling evidence of uniform Li-ion plating on SS, clearly showing the accumulation of Li-ions during charging and depletion of Li-ions during discharging. Figure 4j shows mass to charge ratio of lithium-ion in pristine, charged and discharged state of the μ -battery. Figure 4k presents normalized Li-ion counts versus sputtering time of the μ -battery in pristine, charged, and discharged state; it shows increased Li-ion count on plating and decreased Li-ion count during stripping. The result is presented along with SEM cross-section image of the μ -battery to give more visualization of Li-ion distribution and detailed identification of each layer of the μ -battery, thus starting with SS layer which is composed of multifunctional current collector (CC) anode active material (AAM) layer, followed by solid electrolyte interface/solid electrolyte layer (SEI/SE), then cathode active material (CAM) layer, and final layer of CC and substrate SiO₂/Si.

In Figure S4, Supporting Information, 3D ToF-SIMS of key elements is presented in the 1st row pristine, 2nd row charged, and 3rd row discharged. The 3D images give a clear view of individual ions in each layer of the μ -battery. The ion-segments like Cr, NiO, and C are evenly distributed in the SS layer; this indicates the transformation of purely metallic SS elements into an amorphous mix of evenly distributed carbon, metal, and metal oxide during low-temperature sputtering of SS. This further confirms the successful transformation of the structural element into multifunctional elements that can easily store lithium ions. In addition, the presence of uniformly distributed ions from SE and CAM is confirmed.

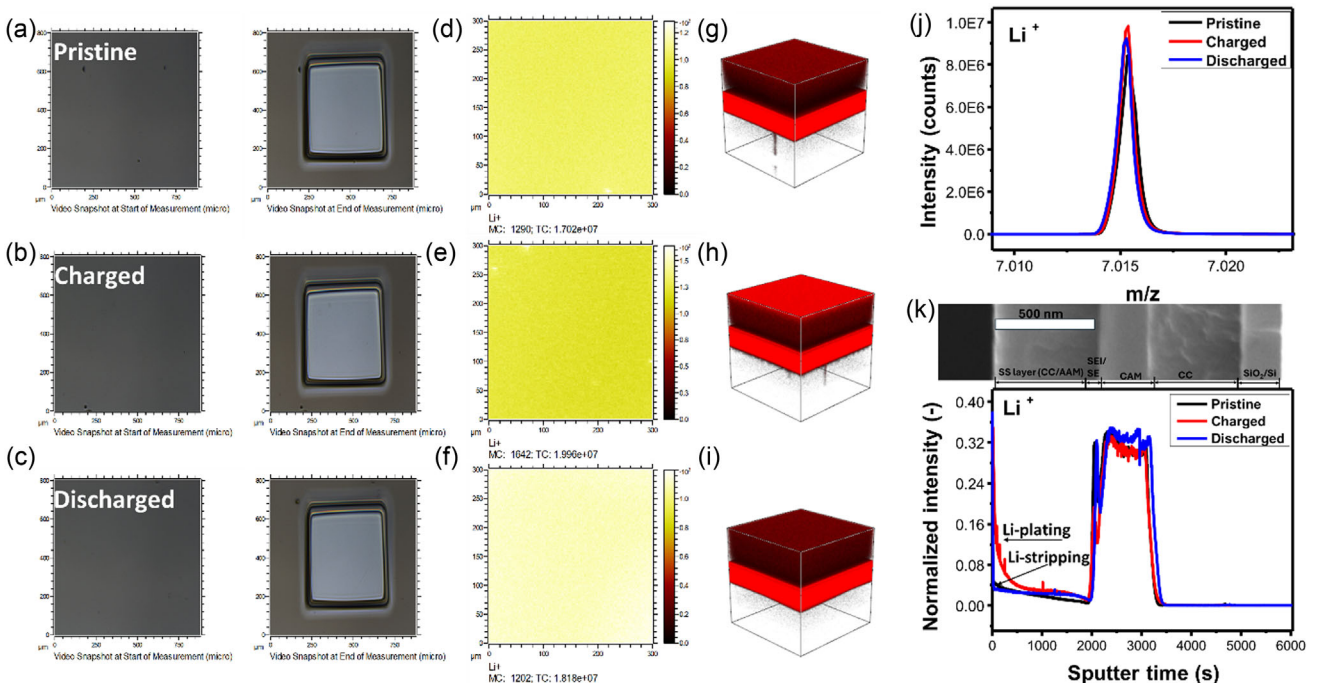


Figure 4. a–c) Video snapshot images $900 \mu\text{m}^2$ area of pristine, charged, and discharged μ -battery before and after sputter via Cs-2Kev ions to acquire ToF-SIMS spectra. d–f) 2D and g–i) 3D, ToF-SIM of Li-ion in pristine, charged, and discharged states. j) Mass to charge ratio versus intensity of Li-ion in pristine, charged, and discharged states. k) ToF-SIMS Li-ion in pristine, charged, and discharged states showing Li-ion plating and stripping.

3. Conclusion

Breaking the long-standing tradition of using SS only as a structural element in the battery; SS encapsulated and enabled all solid-state μ -battery fabricated by layer-by-layer rf-sputtering. The transition of SS from a structural element to multifunctional element was enabled by room temperature rf-sputtering of SS. Which led to the formation of amorphous SS layer composed of carbon, metal, and metal oxide, providing both electrical conductivity and the ability to host Li-ion. The battery architecture used is as simple as it gets; equivalent SS current collectors served both as current collectors and anode of the battery. The battery is realized on commercial silicon wafer for possible integration with microelectronic systems. Furthermore, components used in the battery are among the commonly used cheap battery elements. The real-time test of the battery using red 630 nm LED and as well as electrochemical techniques presents compelling evidence of the battery's operation. In addition, probing the μ -battery using ToF-SIMS confirmed the successful Li-ion plating/stripping on amorphous SS during cycling. Furthermore, effective encapsulation of the battery active elements contributed to the stability of the battery. We believe this work presents simple, cheap, and practical μ -battery which can easily be integrated into applications requiring low and intermittent power.

4. Experimental Section

Radio frequency (RF) magnetron sputtering was conducted using SS target (SUS316 iTASCO, Item No. TSUSEM0012), lithium iron phosphate target (LiFePO_4 iTASCO, Item No. TLIACR0010), and lithium

phosphate target (Li_3PO_4 MSE Supplies Batch. 25522A4). A cleaned silicon wafer with an oxide overlayer of 200 nm was covered with a lab-made aluminum mask (T-shaped with rectangular top and a short vertical arm) and loaded into the sputtering chamber followed by pumping the chamber to $(2 \times 10^{-5} \approx 4 \times 10^{-5})$ Torr. Then the targets were presputtered for clean-up for several minutes. The deposition was carried out in Ar and O_2 for Li_3PO_4 and in Ar for steel and LiFePO_4 . The pressure varied from 5 to 10 mTorr and sputtering power was varied from 100 to 150 W for 1 h to 6 h and temperature of RT ($\approx 23^\circ\text{C}$) to 30 °C. In between each sputtering step, the chamber was vented, the sputtering target was changed, and the samples were handled in ambient conditions to make an additional mask for the subsequent layer. The sputtering sequence is as follows: SS, LiFePO_4 , Li_3PO_4 , and SS. To optimize the ionic conductivity of Li_3PO_4 , SS layer was deposited at RT followed by the deposition Li_3PO_4 at (RT, 10 °C, 20 °C, and 30 °C), and then SS layer was deposited as final layer at RT forming equivalent current collectors.

The structure, morphology, lattice vibration modes, and in-depth chemical composition of the samples was investigated using XRD (Rigaku, Ultima III, monochromated $\text{CuK}\alpha$ radiation; scan rate: 4°/min, Japan), Raman microscopic system (a 300M+, WITec) with a pump laser wavelength of 532 nm, SEM (JEOL, JSM IT500HR, Accelerating voltage: 5 kV, Japan), and Time of Flight Secondary Ion Mass Spectrometer (ToF-SIMS, TOF-SIMS 5, ION-TOF GmbH) with primary ion of Bi_1^+ and acceleration voltage of 30 keV at the KBSI, Busan Center (PH412), respectively.

Electrochemical measurements were conducted in a two-electrode system with an electrochemical analyzer (IVIUM Technologies) in ambient condition. Electrochemical impedance spectroscopy (EIS) measurements were performed under an ac bias of 10 mV in the frequency range of 10 MHz to 0.1 Hz to obtain charge transfer resistance. CV tests were performed at a scan rate ranging from 1 to 5 mV s^{-1} to obtain the electrochemical stability window and redox peaks. Galvanostatic charge-discharge (GCD) data was obtained by applying constant current calculated from theoretical

capacity of the battery to determine the actual capacity and stability of the battery. For instance, 600 nm of LFP in an area of 2.25 cm^{-2} has a mass of $4.68 \mu\text{g}$ and results in $1\text{C} = 0.8 \mu\text{Ah}$.

Acknowledgements

This work was supported by the National Research Foundation of Korea (NRF) grant funded by the Korea government (MSIT) (No. RS-2023-00208311).

Conflict of Interest

The authors declare no conflict of interest.

Data Availability Statement

The data that support the findings of this study are available from the corresponding author upon reasonable request.

Keywords: amorphous stainless steels · anode free · layer-by-layer-sputtering · Li-ion batteries · microbatteries · solid-state batteries

- [1] M. Zhu, O. G. Schmidt, *Nature* **2021**, *589*, 195.
- [2] T. Wu, W. Dai, M. Ke, Q. Huang, L. Lu, *Adv. Sci.* **2021**, *8*, 2100774.
- [3] Q. Xia, F. Zan, Q. Zhang, W. Liu, Q. Li, Y. He, J. Hua, J. Liu, J. Xu, J. Wang, C. Wu, H. Xia, *Adv. Mater.* **2023**, *35*, 2200538.
- [4] R. H. Brugge, R. J. Chater, J. A. Kilner, A. Aguadero, *JPhys Energy* **2021**, *3*, 034001.
- [5] Q. Zhao, Y. Deng, N. W. Utomo, J. Zheng, P. Biswal, J. Yin, L. A. Archer, *Nat. Commun.* **2021**, *12*, 6034.
- [6] A. C. Kozen, A. J. Pearse, C. F. Lin, M. Noked, G. W. Rubloff, *Chem. Mater.* **2015**, *27*, 5324.
- [7] T. Ohnishi, K. Takada, *ACS Omega* **2022**, *7*, 21199.
- [8] H. D. Lim, J. H. Park, H. J. Shin, J. Jeong, J. T. Kim, K. W. Nam, H. G. Jung, K. Y. Chung, *Energy Storage Mater.* **2020**, *25*, 224.
- [9] Y. K. Sun, *ACS Energy Lett.* **2020**, *5*, 3221.
- [10] J. Sastre, X. Chen, A. Aribia, A. N. Tiwari, Y. E. Romanyuk, *ACS Appl. Mater. Interfaces* **2020**, *12*, 36196.

- [11] A. Aribia, J. Sastre, X. Chen, M. H. Futscher, M. Rumpel, A. Priebe, M. Döbeli, N. Osenciat, A. N. Tiwari, Y. E. Romanyuk, *Adv. Energy Mater.* **2022**, *12*, 4.
- [12] S. Sun, Z. Han, W. Liu, Q. Xia, L. Xue, X. Lei, T. Zhai, D. Su, H. Xia, *Nat. Commun.* **2023**, *14*, 6662.
- [13] J. B. Bates, N. J. Dudney, B. Neudecker, A. Ueda, C. D. Evans, *Solid State Ionics* **2000**, *135*, 33.
- [14] N. J. Dudney, J. B. Bates, J. D. Robertson, *J. Vac. Sci. Technol. A Vacuum, Surfaces, Film.* **1993**, *11*, 377.
- [15] A. A. Talin, D. Ruzmetov, A. Kolmakov, K. McKelvey, N. Ware, F. El Gabaly, B. Dunn, H. S. White, *ACS Appl. Mater. Interfaces* **2016**, *8*, 32385.
- [16] B. Uzakbaiuly, A. Mukanova, Y. Zhang, Z. Bakenov, *Front. Energy Res.* **2021**, *9*, 1.
- [17] T. Koç, F. Marchini, G. Rousse, R. Dugas, J. M. Tarascon, *ACS Appl. Energy Mater.* **2021**, *4*, 13575.
- [18] J. Li, J. Qi, F. Jin, F. Zhang, L. Zheng, L. Tang, R. Huang, J. Xu, H. Chen, M. Liu, Y. Qiu, A. I. Cooper, Y. Shen, L. Chen, *Nat. Commun.* **2022**, *13*, 2031.
- [19] W. Z. Huang, Z. Y. Liu, P. Xu, W. J. Kong, X. Y. Huang, P. Shi, P. Wu, C. Z. Zhao, H. Yuan, J. Q. Huang, Q. Zhang, *J. Mater. Chem. A* **2023**, *11*, 12713.
- [20] H. Song, J. Lee, M. Sagong, J. Jeon, Y. Han, J. Kim, H. G. Jung, J. S. Yu, J. Lee, I. D. Kim, *Adv. Mater.* **2024**, *36*, 2407381.
- [21] H. Pan, L. Wang, Y. Shi, C. Sheng, S. Yang, P. He, H. Zhou, *Nat. Commun.* **2024**, *15*, 2263.
- [22] Y. Liu, X. Meng, Z. Wang, J. Qiu, *Nat. Commun.* **2022**, *13*, 4415, <https://doi.org/10.1038/s41467-022-32031-7>.
- [23] Y. Wang, Y. Liu, M. Nguyen, J. Cho, N. Katyal, B. S. Vishnugop, H. Hao, R. Fang, N. Wu, P. Liu, P. P. Mukherjee, J. Nanda, G. Henkelman, J. Watt, D. Mitlin, *Adv. Mater.* **2023**, *35*, 8, 202206762.
- [24] L. X. Yuan, Z. H. Wang, W. X. Zhang, X. L. Hu, J. T. Chen, Y. H. Huang, J. B. Goodenough, *Energy Environ. Sci.* **2011**, *4*, 269.
- [25] S. Yuan, Q. Lai, X. Duan, Q. Wang, *J. Energy Storage* **2023**, *61*, 106716.
- [26] A. A. Abde-Hamid, A. Mendoza-Garcia, S. S. Lee, J. Y. Ying, *Nano Energy* **2024**, *119*, 109025.
- [27] T. Kreher, F. Heim, J. Pross-Brakhage, J. Hemmerling, K. P. Birke, *Batteries* **2023**, *9*, 412.
- [28] S. Saha, K. L. Routray, D. Behera, *Trans. Electr. Electron. Mater.* **2023**, *24*, 295.
- [29] S. Naeem, *Trans. Electr. Electron. Mater.* **2024**, *25*, 589.
- [30] S. K. Sourav, S. K. Parida, R. N. P. Choudhary, U. Prasad, *Trans. Electr. Electron. Mater.* **2023**, *24*, 434.
- [31] B. Dash, K. L. Routray, S. Saha, S. Yoshimura, S. Ratha, M. K. Rout, *Trans. Electr. Electron. Mater.* **2024**, *25*, 232.
- [32] D. Qu, W. Ji, H. Qu, *Commun. Mater.* **2022**, *3*, 1.

Manuscript received: May 2, 2025

Revised manuscript received: July 3, 2025

Version of record online: